Approximate Methods for Simulating Optical Properties of Plasmonic Nanoparticle Assemblies

Kenny K. Lam

A thesis
submitted in partial fulfillment of the
requirements for the degree of

Master of Science

University of Washington
2025

Committee:
Zachary M. Sherman
Lilo D. Pozzo

Program Authorized to Offer Degree:
Chemical Engineering

University of Washington

Abstract

Approximate Methods for Simulating Optical Properties of Plasmonic Nanoparticle Assemblies

Kenny K. Lam

Chair of the Supervisory Committee:

Zachary M. Sherman

Department of Chemical Engineering

Simulating optical responses of plasmonic nanoparticle assemblies is a crucial milestone for advancing the design and optimization of optical metamaterials and photonic devices. Since optical responses are highly dependent on light frequencies sampled on particle structures, simulations often iterate its calculation on small increments of frequencies to preserve high resolution for the resulting spectra, leading to a high computational cost. In this thesis, we introduce the Kramers-Kronig resonance frequency (KK-res) approximation. KK-res only requires two particle dipole calculations at low- and high-frequency limit, rather than particle dipoles at each frequency, to estimate the full extinction spectra of large particle configurations ($N > 10^4$). This allows KK-res to gain an order-of-magnitude computation time improvement comparing to other coarse-grained mutual dipoles methods. Several experimental studies were also simulated with KK-res to gauge the accuracy and utility under conditions like various anisotropic structures and dielectric models.

Contents

1 Introduction

Nanophotonic materials are consisted of colloidal scale particles ($10 - 100\,\mathrm{nm}$) and interact with light whose wavelength is much larger than the particle sizes. Based on the composite particle types, they can also be classified as plasmonic and dielectric materials. Plasmonic materials are usually composed of metallic (e.g., gold and silver) nanoparticles and exhibit localized surface plasmon resonance (LSPR) when exposed to light. LSPR happens in nanoparticles that have free electrons dispersed in the conductive bands of the surface plasmons. Incident light excites collective oscillations that resonate at specific wavelengths, leading to different optical responses like light absorption and scattering. [1] On the other hand, dielectric materials are made of polarizable nanoparticles (e.g., silicon and titanium dioxide) and generate a constant polarization of electrons that is independent of light wavelength. [2] Since the optical properties of plasmonic materials are highly tunable due to their dependency on the particle structure in the material, particle type, and particle composition, scientists are more interested in applying them as various system components in therapeutics, spectroscopy, sustainable energy, etc. [3–5] Therefore, plasmonic materials are the focus in this thesis. To control the dielectric properties of plasmonic nanoparticles, we alter the element type used and their composition percentage in the colloid. Techniques such as impurity doping are specialized in achieving this goal in experiments. [6] Particle structure is governed by more factors such as interparticle interactions and particle concentration. Top-down and bottom-up fabrications are the two experimental methods to generate plasmonic nanoparticle assemblies for characterizing their optical properties. [7, 8]

High tunability gives freedom to us to engineer plasmonic metamaterials whose light-matter interaction is not possible in natural materials. However, it introduces an important problem when optimizing the metamaterial: with a multi-dimensional parameter space, an exhaustive search of the optimal plasmonic material with experiment becomes infeasible. Hence, scientists built different optical simulation models (e.g., finite-difference time-domain and finite element method) that describe the underlying physics behind observed phenomena in experiments. An example of phenomenon is the reddening effect. An assembly of plasmonic nanoparticles will resonate

at higher light wavelength (lower light frequency) as their concentration in the solvent increases, which is equivalent to decreasing interparticle distances. [9] Nonetheless, due to the frequency-dependent nature of optical properties, to reproduce any spectra (optical property as a function of light frequency), a simulation is required to iterate its calculation with small increments of light frequencies. Thus, traditional simulation methods are not suitable for material optimization because computing the full, high-resolution spectrum takes a long computational time. In this thesis, we propose a new approximate method, Kramers-Kronig resonance frequency (KK-res) approximation, which addresses this issue. The general idea is that we will predict individual optical responses with only measurements at two frequencies at low and high limit; then, compute the full spectrum based on them. The full formulation of method is highlighted in Section 3.2. In the same Chapter 3, we also discuss two optical simulation methods: mutual polarization method (MPM) and Maxwell-Garnett effective medium (mean-field) approximation. MPM is a coarse-grained mutual dipole approximation which is designated for colloidal optical simulations. [10]. Mean-field approximation is an analytic solution which assumes nanoparticles in the system are blended into an isotropic "effective medium" and calculates optical responses on it, implying that mean-field has no local particle structure information.

To verify the integrity of our KK-res approximation, multiple simulation studies are conducted. In Section 4, we compare the total runtime for the same workload between KK-res and MPM, highlighting the strength of KK-res. In Section 5, we look at particle dispersions assembled with various "sticky" force strength and confirm that KK-res can capture optical phenomena shown by other simulation methods and theories. In Section 6, we follow an experimental study on two-dimensional superlattices composed of plasmonic and dielectric nanoparticles. It displays the extensibility of KK-res to other measured optical properties. Finally, in Section 7, we apply the KK-res workflow on a different dielectric model. It verifies that our assumptions still hold in other basis and shows the versatility of the KK-res method.

2 Brownian Dynamics Simulation

Creating correct plasmonic nanoparticle assemblies is the most important initial step to analyze their optical properties. Like in experiments, without a sample, there is nowhere to start the research project. In this thesis, we use a Langevin-type model to govern how the particle positions are updated as the simulation time passes. The model explicitly shows each colloid particle as a discrete sphere and treats the background solvent implicitly as a Newtonian fluid continuum. Hence, only the effects of the solvent on the particles is accounted. They include the hydrodynamic forces from fluid flows and stochastic Brownian forces from fluctuating interactions between the colloids and solvent molecules. [11]

In our simulations, we have a monodisperse suspension of N spherical colloid particles of radius a and mass m dispersed in a fluid of viscosity η. The Langevin equation governs the dynamics of particle i at a position $\mathbf{x}_i(t)$ at simulation time t [12]

$$m\frac{d^2\mathbf{x}_i}{dt^2} = \mathbf{F}_i^H + \mathbf{F}_i^B + \mathbf{F}_i^I \tag{1}$$

where $\mathbf{F}_i^H$ is the hydrodynamic force, $\mathbf{F}_i^B$ is the stochastic Brownian force, and $\mathbf{F}_i^I$ is the interparticle force.

If a force is suddenly applied to a resting colloid particle, the particle accelerates to a terminal velocity over an inertial time scale $\tau_I \equiv m/\gamma_s$, where $\gamma_s \equiv 6\pi\eta a$ is the Stokes drag coefficient. [13] Since we are interested in modeling the equilibrated assembly and their transport, we only concerns with a time scale where particles actually move. One such time scale is for diffusion $\tau_D \equiv \gamma_s a^2/k_BT$, where k_BT is the solvent thermal energy. The Schmidt number $\mathrm{Sc} \equiv \tau_D/\tau_I = \gamma_s^2 a^2/mk_BT$ compares the rate of inertia to the rate of diffusion. For typical colloids of size $a \approx 1\,\mu\mathrm{m}$ in water of density $\approx 10^3\,\mathrm{kg/m^3}$ and viscosity $\eta \approx 10^{-3}\,\mathrm{Pa\cdot s}$ at temperature $T \approx 293\,\mathrm{K}$, the Schmidt number if $\mathrm{Sc} \approx 10^7$, indicating that inertial relaxation is orders of magnitude faster than particle motion. If we were to integrate Eq. (1) numerically, a majority of computational effort would be spent resolving the inertial dynamics, and it would be difficult to reach the diffusive

time scale. Therefore, as long as we take simulation time steps larger than τ_I, assuming particles instantaneously move at their terminal velocity when they feel a force is a sufficient condition. In this case, the acceleration of particles is zero and the dynamics are said to be overdamped.

$$0 = \mathbf{F}_i^H + \mathbf{F}_i^B + \mathbf{F}_i^I \tag{2}$$

This equation imposes a new problem of lacking velocity terms that are essential to update particle positions. It turns out we can obtain particle velocity through the hydrodynamic forces $\mathbf{F}_i^H$.

2.1 Hydrodynamic Forces

As colloid particles move around in the solvent, solvent molecules will move in the opposite direction along the particle surface to preserve the total volume. Naturally, it means that the hydrodynamic forces on each particle are coupled and long-ranged, but the system can be described by particle velocity $\mathbf{u}_i$ linearly mapping to nonhydrodynamic forces $\mathbf{F}_j \equiv \mathbf{F}_j^B + \mathbf{F}_j^I$

$$\mathbf{u}_i = \sum_j \mathbf{M}_{ij}^H \cdot \mathbf{F}_j \tag{3}$$

where $\mathbf{M}_{ij}^H$ is the hydrodynamic mobility tensor. [13, 14] We can also rewrite Eq. (3) in matrix form for all N particles.

$$\begin{bmatrix} \mathbf{u}_1 \\ \mathbf{u}_2 \\ \vdots \end{bmatrix} = \begin{bmatrix} \mathbf{M}_{11}^H & \mathbf{M}_{12}^H & \cdots \\ \mathbf{M}_{21}^H & \mathbf{M}_{22}^H & \cdots \\ \vdots & \vdots & \ddots \end{bmatrix} \cdot \begin{bmatrix} \mathbf{F}_1 \\ \mathbf{F}_2 \\ \vdots \end{bmatrix} \quad \Rightarrow \quad \mathscr{U} = \mathscr{M}^H \cdot \mathscr{F} \tag{4}$$

where $\mathscr{U} \equiv [\mathbf{u}_1, \mathbf{u}_2, \ldots, \mathbf{u}_N]^T$ is a list of N particle velocities, $\mathscr{F} \equiv [\mathbf{F}_1, \mathbf{F}_2, \ldots, \mathbf{F}_N]^T$ is a list of particle nonhydrodynamic forces, $\mathscr{M}^H$ is the grand hydrodynamic mobility tensor, and the T superscript indicates transposition.[i]

[i] Script letters are used to denote collections of individual particle variables.

To reduce the computational cost of computing the long-ranged, many-bodied hydrodynamic interaction, we implement the "freely draining" model, which neglects interparticle hydrodynamic interactions so that the drag on each particle is decoupled from all of the others and equal to the Stokes drag.

$$\mathbf{M}_{ij}^{H} = 0,\ i \neq j \qquad \mathbf{M}_{ii}^{H} = \mathbf{I}/\gamma_s \tag{5}$$

With this assumption, the relationship in Eq. (3) is simplified as

$$\mathbf{u}_i = \frac{\mathbf{F}_i}{\gamma_s} \tag{6}$$

This equation governs the dynamics of each particle at every simulation time t. It can be numerically integrated over a time step Δt using a forward Euler scheme to update the particle positions.

$$\mathbf{x}_i(t + \Delta t) = \mathbf{x}_i(t) + \frac{1}{\gamma_s}\mathbf{F}_i(t)\Delta t \tag{7}$$

This discretized version is the one implemented in simulations. With the knowledge of current particle positions $\mathbf{x}_i(t)$, we can update the positions after some $\Delta t > \tau_I$ using the nonhydrodynamic forces $\mathbf{F}_i$ exerted on particles at simulation time t.

2.2 Brownian Forces

The solvent exerts stochastic Brownian forces on the particles from the random collisions of solvent molecules onto the colloids. It is a fluctuating interaction and is governed by the statistics of the fluctuation-dissipation theorem. [13]

$$\left\langle \mathscr{F}^B(t) \right\rangle = 0, \quad \left\langle \mathscr{F}^B(t)\mathscr{F}^B(t+\tau) \right\rangle = 2k_B T(\mathscr{M}^H)^{-1}\delta(\tau) \tag{8}$$

where δ is the Dirac δ-function and $\langle\cdot\rangle$ is an ensemble average over particles and time. The average Brownian force is always zero, while its variance is related to the inverse of the grand hydrodynamic

mobility tensor as an impulse. The Brownian forces are also uncorrelated in time, so the set of forces $\mathscr{F}^B$ at one time has no effect on the set of forces at any other time and $\delta(\tau)$ can be averaged over a single time step Δt. In addition, we substitute the hydrodynamic mobility $\mathbf{M}_{ij}^H$ of the freely draining model into Eq. (8).

$$\left\langle \mathscr{F}^B \right\rangle = 0, \quad \left\langle \mathscr{F}^B \mathscr{F}^B \right\rangle = \frac{2k_B T \gamma_s \mathbf{I}}{\Delta t} \tag{9}$$

This shows that every colloid particle in a monodisperse system will obtain the same Brownian force.

2.3 Interparticle Forces

Interparticle forces arising from thermodynamic interactions among particles are usually represented as the gradient of potential energy $U(\mathscr{X})$, which is a function of particle positions $\mathscr{X} \equiv [\mathbf{x}_1, \mathbf{x}_2, \ldots, \mathbf{x}_N]^T$.

$$\mathbf{F}_i^I(\mathscr{X}) \equiv -\nabla_{\mathbf{x}_i} U(\mathscr{X}) \tag{10}$$

However, since all the interparticle forces used in this thesis are pairwise, only the relative displacement $\mathbf{r}$ between a pair of particles needs to be take into account. The forces are represented with sums of pairwise forces instead.

$$\mathbf{F}_{ij}^I(\mathbf{r}) \equiv \nabla_{\mathbf{r}} U_{ij}(\mathbf{r}) \tag{11}$$

The first interparticle interaction is the "hard-sphere" potential, which assumes particles are solid, rigid, and cannot overlap with one another. The pair potential function is

$$U_{ij}^{hs} = \begin{cases} \infty & \text{if } r < 2a \\ 0 & \text{if } r \geq 2a \end{cases} \tag{12}$$

Therefore, particle overlaps require an infinite energy and are forbidden. This potential is also non-interacting outside particle overlaps. The hard-sphere force computed by the derivative of this

potential is discontinuous, signaled by the Heaviside step function in Eq. (12). This type of force cannot be directly implemented in simulations. Heyes and Melrose designed a "potential-free" hard-sphere algorithm by allowing particles to temporarily overlap over a part of a full time step due to other forces and then separating them to exactly contact at $r = 2a$ at the end of the time step. [15] Because all forces are explicitly defined and correlated to particle velocity in Eq. (3), the effective hard-sphere force required to separate two overlapping particles to contact can be calculated exactly. Thus, we can write the "potential-free" algorithm in terms of a hard-sphere pair potential. [ii]

$$U_{ij}^{hs} = \begin{cases} \frac{\gamma_s}{4\Delta t}(r-2a)^2 & \text{if } r < 2a \\ 0 & \text{if } r \geq 2a \end{cases} \tag{13}$$

There are no adjustable parameters in this function because particles are brought to exactly touching via Δt over a single time step.

The second interparticle interaction is the "depletion" potential. It is implemented as a tunable, attractive pair potential to create colloidal aggregations. The formulation follows the Asakura-Oosawa model. [16] It assumes each particle has a depletion zone with thickness $\delta < 2a$ around it. As the depletion zones of two particles overlap, fewer solvent molecules exist between their gap, or being "depleted". This creates a difference in osmotic pressure from the gap side and the opposite side of the particle, and thus an attractive, net force between the two particles arises. the functional form of the pair potential is

$$U_{ij}^{dep} = \begin{cases} -U_0 \dfrac{(r-2(a+\delta))^2(r^2+4r(a+\delta))}{16r\delta^3\left(1+\dfrac{3}{2\delta}\right)} & r \leq 2a+2\delta \\ 0 & r > 2a+2\delta \end{cases} \tag{14}$$

where U_0 is the depletion strength.

[ii] "Potential-free" here means the hard-sphere interaction is not parameterized, so the force is not tunable.

2.4 Implementation

All simulations are run in HOOMD-Blue, a software suite with a python application programming interface (API) for particle simulations optimized on graphics processing units (GPUs). [17–19] All calculations in Brownian dynamics simulations are performed on dimensionless quantities, so we must select a set of units to nondimensionalize variables. The basis units are shown in Table 1. A dimensionless version of a variable is indicated with a tilde $\sim$.

Variable	Unit
length	a
energy	$k_B T$
time	$\tau_D = \frac{\gamma_s a^2}{k_B T}$

Table 1: Nondimensional units used in Brownian dynamics simulations.

3 Calculating Optical Responses from Colloidal Assemblies

3.1 Mutual Polarization Method (MPM)

The full derivation of the mutual polarization method (MPM) is explained in the supplement document of the paper by Sherman et al. and the code is available at github.com/zeesherman/mutual-polarization. [10] Plasmonic nanoparticles are defined as particles whose electron density can couple with electromagnetic waves and exhibit a polarization through the resonating surface plasmons. [20] The strength of polarization is characterized by the particle permittivity $\varepsilon_{p,i}(\omega)$ as a function of incident light frequency ω. In reality, there are different polarization modes (e.g. dipole, quadrupole, octupole) for a particle, we will only calculate particle dipoles here because higher orders of polarization are significantly heavier in computations and provide a slight increase on accuracy. Another assumption is that we only consider particles in the quasistatic limit, where particle radius a is much smaller than the wavelength of light sampled, to avoid spatial-dependent effect due to the wave location in particles. To capture the optical responses of a plasmonic nanoparticle assembly, we simulate light waves of various wavelengths shine on a particle configuration and

determine N particle dipole moments $\mathbf{p}_1, \mathbf{p}_2, \ldots, \mathbf{p}_N$ by solving the electrostatic limit of Maxwell's equations.

MPM does exactly that by rapidly computing the far- and near-field optical responses through the unit directional polarizations of each particle by an incident electric field $\mathbf{E}_0$ and by the electric dipoles of the other $N-1$ particles in the system. The electric dipole of particle i, $\mathbf{p}_i = \varepsilon_f \alpha_i(\omega)\mathbf{E}(\mathbf{x}_i)$, is expressed in terms of its dipolar polarizability, $\alpha_i(\omega) = 4\pi a^3(\varepsilon_{p,i}(\omega) - \varepsilon_f)/(\varepsilon_{p,i}(\omega) + 2\varepsilon_f)$, and the local electric field, $\mathbf{E}(\mathbf{x}) = \mathbf{E}_0 + \sum_j^N (4\pi r^3 \varepsilon_f)^{-1}(3\hat{\mathbf{r}}\hat{\mathbf{r}} - \mathbf{I}) \cdot \mathbf{p}_j$, which is a sum of the incident electric field and the scattered field expanded to the lowest order in ω. Here, ε_f is the background fluid permittivity (assumed pure real), $\varepsilon_{p,i}(\omega)$ is permittivity of particle i at frequency ω, $\mathbf{r} = \mathbf{x} - \mathbf{x}_i$, $r = |\mathbf{r}|$, $\hat{\mathbf{r}} = \mathbf{r}/r$, and $\mathbf{I}$ is the identity tensor. Other optical response observables, such as frequency-dependent extinction cross-section $\sigma(\omega)$ or transmittance through a nanoparticle structure, can be readily computed from the dipole result.

Similar to hydrodynamic forces in Section 2.1, the N induced particle dipoles in an electric field $\mathbf{E}_0$ of magnitude $E_0 = |\mathbf{E}_0|$ are computed by solving the linear system of equations for each frequency ω.

$$\mathbf{E}_0 = \sum_j^N \mathbf{M}_{ij} \cdot \mathbf{p}_j \tag{15}$$

where

$$\mathbf{M}_{ij} = \begin{cases} \dfrac{1}{\varepsilon_f \alpha_i}\mathbf{I} & i = j \\ \dfrac{1}{4\pi\varepsilon_f r_{ij}^3}(\mathbf{I} - 3\hat{\mathbf{r}}_{ij}\hat{\mathbf{r}}_{ij}) & i \neq j,\ r_{ij} \geq 2a \\ \dfrac{1}{4\pi a^3 \varepsilon_f}\left[\left(1 - \dfrac{9r_{ij}}{16a} + \dfrac{r_{ij}^3}{32a^3}\right)\mathbf{I} + \left(\dfrac{3r_{ij}^3}{32a^3} - \dfrac{9r_{ij}}{16a}\right)\hat{\mathbf{r}}_{ij}\hat{\mathbf{r}}_{ij}\right] & i \neq j,\ r_{ij} < 2a \end{cases} \tag{16}$$

MPM is constructed to prevent matrix singularities, unphysical property predictions, and convergence issues when solving for dipoles of overlapping colloid particles. Triply periodic boundary condition is usually enforced in simulation to mimic a large system. Since dipole interaction decays very slow $\mathbf{p}_i \sim 1/r^3$ in distance, we cannot cut off the coupling to a particle dipole from another

particle that is far away (including those in periodic images). Therefore, a spectrally accurate Ewald summation is employed to solve Eq. (15) using iterative scheme. [21]

3.2 Kramers-Kronig Resonance Frequency (KK-res) Approximation

Our Kramers-Kronig resonance frequency (KK-res) approximation is motivated from the fact that the ensemble extinction cross-section per nanoparticle volume $\sigma_V(\omega)$ is calculated from the average of individual particle extinction cross-section $\sigma_i(\omega)$. Depending on the particle configuration and the dielectric function, the particle extinction spectra exhibit various features but maintains a certain line shape. Therefore, we could establish a fixed peak function for the extinction cross-section.

$$\sigma_i(\omega) = \frac{h_i}{1 + \left(\frac{\omega_{res,i}}{W_i}\right)^2 \left(\frac{\omega}{\omega_{res,i}} - \frac{\omega_{res,i}}{\omega}\right)^2} \tag{17}$$

where $\sigma_i(\omega)$ is the particle extinction cross-section, h_i is the peak height, $\omega_{res,i}$ is the resonance frequency, W_i is the full width at half-maximum (FWHM) of the most prominent peak. This function originates from the definition of extinction cross-section as a function of the imaginary part of dipoles in the case of isolated Drude particles.

With the mutually coupling polarization among particles, each particle no longer has an equal $\omega_{res,i}$, W_i, and h_i. However, the dipoles must satisfy the Kramers-Kronig relation, which holds for certain complex scalar functions.

$$f'(\omega) = \frac{2}{\pi} P \int_0^\infty d\omega' \, \frac{\omega' f''(\omega')}{\omega'^2 - \omega^2} \tag{18}$$

$$f''(\omega) = -\frac{2\omega}{\pi} P \int_0^\infty d\omega' \, \frac{f'(\omega')}{\omega'^2 - \omega^2} \tag{19}$$

where $f(\omega)$ is an arbitrary complex scalar function, $f'(\omega)$ and $f''(\omega)$ are the real and imaginary part of f, and P is the Cauchy principal value. This relation shows that the real and imaginary part of a complex function are not independent, and allows us to reconstruct the full function with only one part. These relations hold when the analytic continuation $f(z) \to 0$ as a complex number

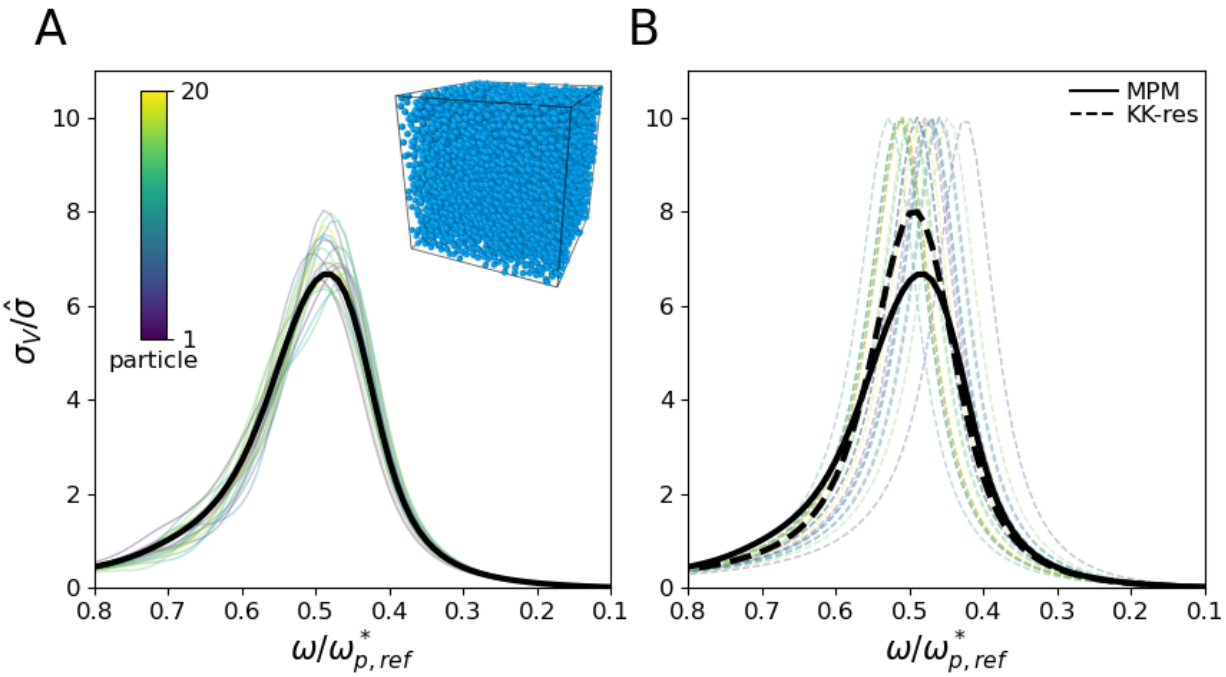

Figure 1: Motivation of KK-res. The extinction spectra of the first 20 particles (solid, colored) from the particle configuration (top-right corner) are shown and the average of them (solid, black) is the ensemble spectrum. As we constrain the lineshape of individual extinction spectra (dashed, colored), the ensemble curve (dashed, black) is still fairly accurate to the solid one. Both extinction cross-section per nanoparticle volume and incident light frequency are nondimensionalized with $\omega^*_{p,ref}$ as the reference effective plasma frequency and $\hat{\sigma} = 4\pi a^3\sqrt{\varepsilon_f\mu_f}\omega^*_{p,ref}/3$ as the unit extinction.

$|z| \to \infty$. [22] Evaluating Eq. (18) at $\omega = 0$, we obtain a "sum rule" result.

$$f'(0) = \frac{2}{\pi}\int_0^\infty d\omega\,\frac{f''(\omega)}{\omega} \tag{20}$$

which expresses the integral of $f''(\omega)$ over all ω to the value of $f'(0)$.

Suppose f is any component C_{ij} of a colloidal suspension's capacitance tensor $\mathbf{C}$, which is the ability of a plasmonic nanoparticle to gain polarizations from coupling with other nanoparticles and the oscillating electric field of the incident light. To demonstrate the derivation, we assume the suspension is isotropic with $\mathbf{C} = C\mathbf{I}$ and composed of Drude particles.

$$\varepsilon_{p,i}(\omega) = \varepsilon_{\infty,i} - \frac{\varepsilon_0\omega_{p,i}^2}{\omega^2 + i\gamma_i\omega} \tag{21}$$

where $\varepsilon_{p,i}(\omega)$ is the particle permittivity, $\varepsilon_{\infty,i}$ is the high-frequency permittivity, $\varepsilon_0 = 8.854 \times 10^{-12}\,\mathrm{F\,m^{-1}}$ is the vacuum permittivity, $\omega_{p,i}$ is the plasma frequency, and γ_i is the damping coefficient. The Drude model leads to a limiting behavior for the single particle capacitance $C_i(\omega) = 4\pi a_i^3 \varepsilon_f \alpha_i$, where $\alpha_i = (\varepsilon_{p,i}(\omega) - \varepsilon_f)/(\varepsilon_{p,i}(\omega) + 2\varepsilon_f)$ is the particle polarizability and ε_f is the permittivity of background fluid.

$$C_i(0) = 4\pi a_i^3 \varepsilon_f \tag{22}$$

$$C_i(\infty) = 4\pi a_i^3 \varepsilon_f \alpha_{\infty,i} \tag{23}$$

where $\alpha_{\infty,i} = (\varepsilon_{\infty,i} - \varepsilon_f)/(\varepsilon_{\infty,i} + 2\varepsilon_f)$. Note that both of these values are pure real. The function $C_{D,i}(\omega) = C_i(\omega) - C_i(\infty)$ will vanish at $\omega \to \infty$ and therefore obeys the Kramers-Kronig relation. This only affects the real part of the Kramers-Kronig relation. We can apply the sum rule Eq. (20) to the capacitance function.

$$\begin{aligned} C'_{D,i}(0) &= \frac{2}{\pi}\int_0^\infty d\omega\, \frac{C''_{D,i}(\omega)}{\omega} \\ C'_i(0) - C'_i(\infty) &= \frac{2}{\pi}\int_0^\infty d\omega\, \frac{C''_i(\omega) - C''_i(\infty)}{\omega} \\ C_i(0) - C_i(\infty) &= \frac{2}{\pi}\int_0^\infty d\omega\, \frac{C''_i(\omega)}{\omega} \end{aligned} \tag{24}$$

The extinction cross-section of particle i is proportional to the imaginary part of its capacitance,

$$\sigma_i(\omega) = \frac{\sqrt{\mu_f}}{\sqrt{\varepsilon_f}}\omega C''_i(\omega) \tag{25}$$

where μ_f is the permeability of background fluid. Rearrange Eq. (25) and plug into Eq. (24).

$$C_i(0) - C_i(\infty) = \frac{2\sqrt{\varepsilon_f}}{\pi\sqrt{\mu_f}}\int_0^\infty d\omega\, \frac{\sigma_i(\omega)}{\omega^2} \tag{26}$$

Here, $\sigma_i \geq 0$ is always nonnegative, so this constrains the local surface plasmon resonance (LSPR) frequency, height, and width – they cannot all be varied independently. If $C_{D,i}(0)$ increases, the

LSPR frequency can red-shifted to lower frequencies so that the denominator of Eq. (24) becomes smaller, increasing the integrand. The LSPR peak height and width can also increase, with broadening to lower frequencies increasing the integral more than broadening to higher frequencies because of the ω denominator. This implies that increasing the imaginary polarization around some frequencies requires decreasing the polarization around others, since the integrand cannot get arbitrarily large everywhere.

Applying the peak function Eq. (17), we obtain an equation that is independent of ω but describes the extinction spectrum.

$$C_i(0) - C_i(\infty) = \frac{\sqrt{\varepsilon_f}}{\sqrt{\mu_f}} \frac{h_i W_i}{\omega_{res,i}^2} \tag{27}$$

This equation isn't helpful as is because we don't know what h_i, W_i, and $\omega_{res,i}$ are. However, we could approximate that the peak width remains unchanged and that the height is a function of the resonance frequency as:

$$W_i = \gamma_i \tag{28}$$

$$h_i = \frac{4\pi a_i^3}{3} \frac{\sqrt{\varepsilon_f \mu_f}\omega_{p,i}^{*2}}{W_i} \left(1 + \left(1 - \frac{\varepsilon_{\infty,i}}{\varepsilon_f}\right)\left(\frac{\omega_{res,i}}{\omega_{p,i}^*}\right)^2\right)^2 \tag{29}$$

where a_i is the particle radius and $\omega_{p,i}^* = \sqrt{\varepsilon_0/\varepsilon_f}\omega_{p,i}$ is the effective plasma frequency. Therefore, $\omega_{res,i}$ is now the only free parameter, and Eq. (27) establishes a relation between $\omega_{res,i}$ and $C_i(0) - C_i(\infty)$.

$$\omega_{res,i} = \omega_{p,i}^* \sqrt{\frac{2}{\chi_i + 2\left(\frac{\varepsilon_{\infty,i}}{\varepsilon_f} - 1\right) + \sqrt{\chi_i^2 + 4\chi_i\left(\frac{\varepsilon_{\infty,i}}{\varepsilon_f} - 1\right)}}} \tag{30}$$

where $\chi_i = (C_i(0) - C_i(\infty))/\frac{4}{3}\pi a_i^3 \varepsilon_f$. By measuring $C_i(0)$ and $C_i(\infty)$, we can use Eq. (30) to get the $\omega_{res,i}$ of each particle. Then, we use the approximations in Eq. (28) and (29) to get W_i and h_i. Finally, we will have $\sigma_i(\omega)$ from the peak function Eq. (17) and therefore $\sigma_V(\omega)$.

3.3 Maxwell-Garnett Effective Medium (Mean-field) Approximation

Maxwell-Garnett effective medium (mean-field) approximation is an analytic solution for the capacitance tensor of a multicomponent nanoparticle mixture.

$$C_i = 4\pi a_i^3 \varepsilon_f \alpha_{mf,i}, \quad \alpha_{mf,i} = \frac{\alpha_i}{1 - \sum_j \alpha_j \phi_j} \tag{31}$$

where ϕ_j is the volume fraction of particles of type j. Applying this definition to Eq. (30), (29), and (17), we will obtain the mean-field expressions of peak features.

$$\omega_{res,i} = \omega_{p,i}^* \sqrt{\frac{1-\phi}{2 + \frac{\varepsilon_{\infty,i}}{\varepsilon_f} + \left(1 - \frac{\varepsilon_{\infty,i}}{\varepsilon_f}\right)\phi}}, \; h_i = \frac{9\sqrt{\varepsilon_f \mu_f}\omega_{p,i}^{*2}}{\gamma_i \left(2 + \frac{\varepsilon_{\infty,i}}{\varepsilon_f} + \left(1 - \frac{\varepsilon_{\infty,i}}{\varepsilon_f}\right)\phi\right)^2}, \; W_i = \gamma_i \tag{32}$$

where ϕ is the colloid volume fraction. These equations are exact for cubic superlattices in the dipole limit. So it is guaranteed that KK-res is as accurate as the mean-field approximation, but with an advantage of capturing structure-dependent and particle-level information. On the other hand, the drawback of KK-res is that all Drude nanoparticles have $\alpha = 1$ in the electrostatic limit. An electrostatic measurement alone is not sufficient to distinguish between Drude nanoparticles with different parameters, so Eq. (30) does not better than mean-field in accounting for compositional heterogeneity. Though, it still can combine structural heterogeneity with mean-field-like compositional variation.

3.4 Nondimensionalization in Optical Simulations

With our focus on optical properties and the nature of simulations in nondimensionality, we introduce a new set of unit for variables used in this thesis. Typical values of these variables are $\omega_{p,ref}^* = 10000\,\mathrm{cm}^{-1}$ and $\varepsilon_f = 1 - 2.5$ for polymer ligands.

Variable	Unit
incident light frequency ω	$\omega^*_{p,ref}$
plasma frequency $\omega_{p,i}$	$\omega^*_{p,ref}$
damping coefficient γ_i	$\omega^*_{p,ref}$
particle permittivity $\varepsilon_{p,i}$	ε_f
particle capacitance C_i	$a^3\varepsilon_f$

Table 2: Nondimensional units used in optical simulation methods

4 Computation Time Improvement

Since MPM computes optical extinction on the spectra at multiple frequencies and KK-res only requires particle dipoles at low- and high-frequency limit to achieve the same goal. We compare the difference in computation time with these two strategies. Here, we ran a Brownian dynamics simulation introduced in Section 2 through 10^7 sampling time steps. The parameters of depletion force are $U_0 = 8$ and $\delta = 0.1$. It means that the attractive force between colloid particles is very strong and so the generated configuration assembles into an arrested gel of nanoparticles, demonstrated in Figure 2. [11] The small depletion zone thickness defines depletion force as a short-range interaction. Therefore, the impact from interparticle forces are completely localized. For particle dielectric properties, we assume they are all pure Drude particles with $\widetilde{\omega}^*_{p,i} = 1$, $\widetilde{\gamma}_i = 0.1$, and $\widetilde{\varepsilon}_{\infty,i} = 2$.

Then, we take 40 frames of particle configuration from the simulation and treat them as different "samples" whose optical properties are needed. MPM and KK-res are applied separately to obtain full extinction spectra. To allocate computational resources for the methods, we use a compute node of 40 central processing unit (CPU) cores and distribute one configuration frame for each CPU core. On each CPU core, MPM calculates particle dipoles at 100 frequencies ranged from $\widetilde{\omega} = 0$ to $\widetilde{\omega} = 0.79$ while KK-res calculates particle dipoles at 2 frequencies, $\widetilde{\omega} = 0$ and $\widetilde{\omega} = \infty$. This setup ensures that both methods accomplish the same amount of work (output 40 extinction spectra with parallel computing) and the computation time reflects what we would see in a realistic simulation study.

KK-res displays a significant computation time improvement comparing to MPM. From Figure

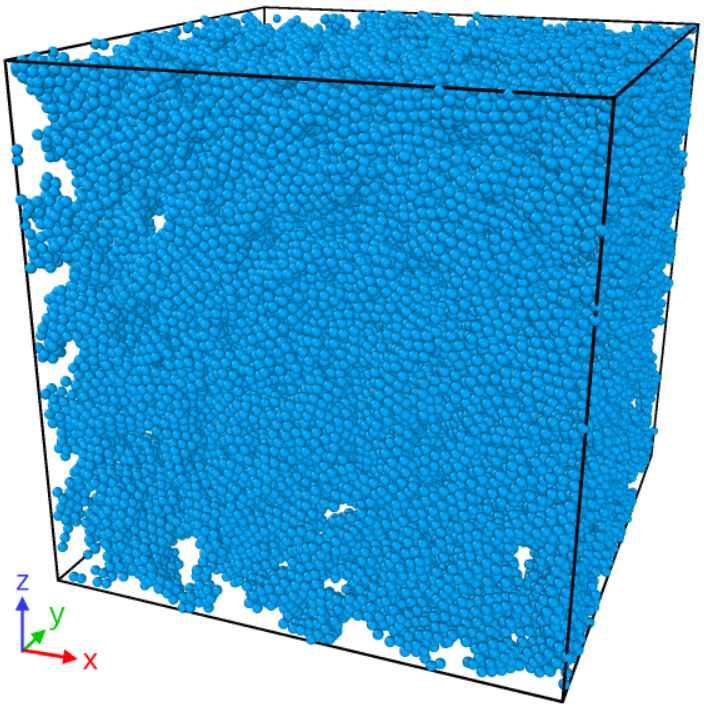

Figure 2: A configuration frame of a simulated particle gel consisted of 64000 particles interacting with hard-sphere and depletion forces at volume fraction $\phi = 0.25$. The strength of depletion force is $U_0 = 8$ and the depletion zone thickness is $\delta = 0.1$.

3, computation time of both methods scales linearly with the number of simulated particles. With MPM sampling 50 times more frequency numbers than KK-res, we would expect the time difference is also 50 times. However, in reality, the calculation of particle dipoles around the resonant frequency ω_{res} is the dominating step for MPM. Since low- and high-frequency limits are never the resonant frequency, KK-res avoids the high computational cost and displays a > 80 times runtime improvement. In addition, gel-like structure is one of the hardest cases to compute the particle dipoles of due to the heterogeneous local environment. Following the linear extrapolation, MPM would take a month to calculate the case of $N = 10^6$ even using HPC resources. Hence, it demonstrates that the KK-res can at least provide insight on structural-dependent impact on extinction cross-section comparing to infeasible information from other methods.

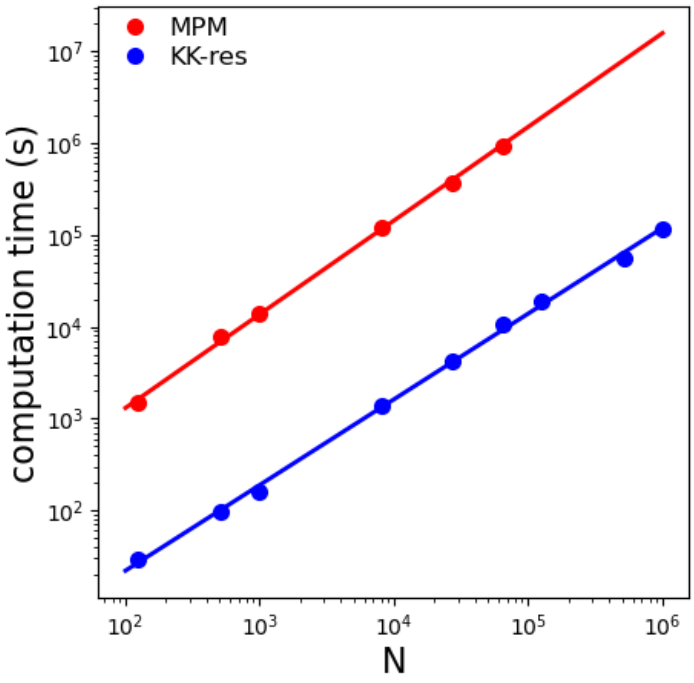

Figure 3: Computation time to calculate the extinction spectra of 40 three-dimensional arrested gel configurations of plasmonic nanoparticles at volume fraction $\phi = 0.25$. Particles attract one another with depletion force whose strength is $U_0 = 8$ and depletion zone thickness is $\delta = 0.1$. The dielectric property is described by Drude model. MPM samples across 100 frequencies and KK-res only samples the low- and high-frequency limit. Both calculations are performed using high-performance computing (HPC) resources on Klone at UW Hyak Research Computing. $N \leq 64000$ are calculated with 2x Intel Xeon Gold 6230 "Cascade Lake" (40 cores), and $N > 64000$ are calculated with 1x AMD EPYC 9654 "Genoa" (40 cores), which has more available memory.

5 Coupling Effect in Dispersions with Weakly Attracted Force

To further showcase the utility of KK-res in simulating plasmonic nanoparticle assemblies, we analyze the extinction spectra of particle configurations assembled with low depletion strengths. In this study, we ran Brownian dynamics simulations with 8000 particles at volume fraction $\phi = 0.25$ with $U_0 = 0,\ 2,$ and 3 and $\delta = 0.1$. Particles are attracted to one another slightly in this case, resulting in a concentrated dispersion configuration, which behaves like liquid but includes temporary, local aggregations. We again use the Drude model to define the dielectric property of each nanoparticle equally. The parameters are $\widetilde{\omega}_{p,i}^{*} = 1$, $\widetilde{\gamma}_i = 0.1$, and $\widetilde{\varepsilon}_{\infty,i} = 1$. This particular system is formulated to demonstrate that KK-res can capture the coupled polarization induced by local structural differences, which is a known optical phenomenon. [9] Therefore, we compute

the ensemble extinction spectra of the average of 10 configuration frames with MPM, KK-res, and mean-field approximation at different depletion strengths, and the resonance frequency and FWHM across multiple colloid volume fractions ϕ.

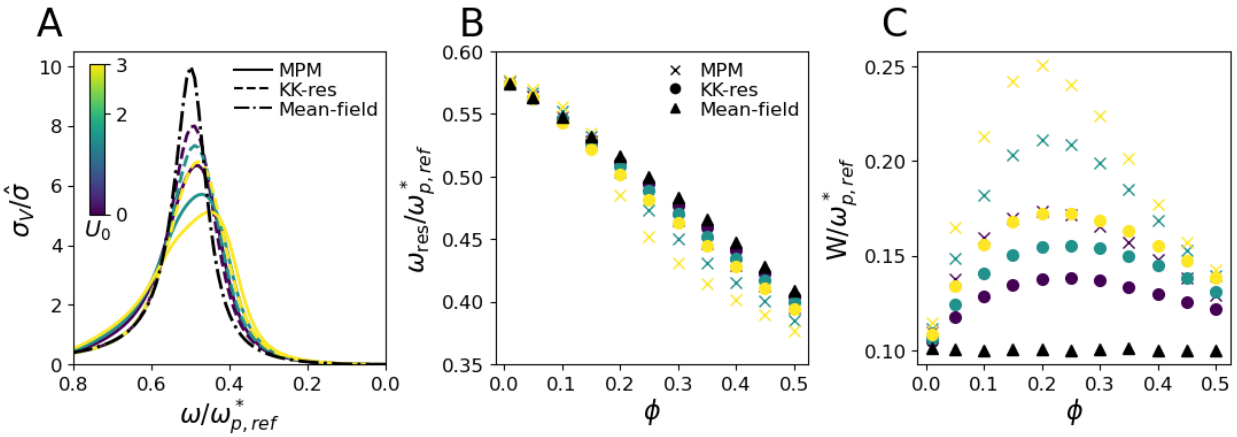

Figure 4: (A) Ensemble extinction spectra of particle configurations assembled at different depletion force strength U_0 (colors) and computed with MPM (solid), KK-res (dashed), and mean-field approximation (black, dot-dashed) at colloid volume fraction $\phi = 0.25$. (B) Ensemble resonance frequency and (C) full width at half-maximum (FWHM) at various volume fraction of plasmonic nanoparticles ϕ.

According to Mie theory, ss interparticle distances decrease between two plasmonic nanoparticles, they will be more "coupled" and resonating at a higher frequency (lower wavelength), so the resonant frequency is "red-shifted". Ways to shrink interparticle distance include increasing volume fraction and tuning up attractive interparticle forces. Coupled particles also significantly increase the ensemble extinction cross-section because more incident light energy is consumed by the plasmon resonance, leading to a higher absorption and scattering of light. In Figure 4A, it shows that both MPM and KK-res capture the red-shift effect while mean-field is invariant with increasing depletion strength. It is because mean-field approximation does not have any particle structure information with the isotropic coarse-grained assumption.

As mentioned, increasing volume fraction is another method to induce more coupling in the structure. In Figure 4B, all 3 approximate methods illustrates the reddening effect. MPM and KK-res achieve this by knowing the each particle position, but mean-field is through Eq. 31 where volume fraction is the only structural variable. Nevertheless, FWHM of the most prominent peak depends on the local structural variations which contributes to the ensemble width. Hence, in

Figure 4C, mean-field approximation displays a constant width $\widetilde{W} = \widetilde{\gamma}_i = 0.1$, which is also an assumption used in KK-res, but MPM and KK-res generates a promising result even with different depletion strengths.

The discrepancy between MPM and KK-res is most likely due to the fact that KK-res always assumes nanoparticles having the same FWHM correlated to the damping coefficient γ_i. We have observed a peak widening effect in Figure 4C on intermediate volume fractions. Therefore, a more systematic function might be applied here to provide a better prediction and improve the accuracy of KK-res.

6 Simulating an Experimental Study of 2D Superlattices

The next example is to reproduce a published experimental study by simulating with KK-res. Kim et al. fabricated close-packed, two-dimensional hexagonal superlattices composed of indium oxide (In_2O_3), a dielectric nanocrystal, and 3% tin-doped indium oxide (3% ITO), a plasmonic nanocrystal, in different mixing ratio. [23] Then, they measured effective refractive index, transmittance, and reflectance of the superlattice sample with an incident light perpendicular to the surface.

In our simulation, we construct a close-packed, two-dimensional perfect hexagonal lattice with area fraction $\phi_A = 0.73$ computationally. The dielectric properties of IO and 3% ITO are given in the experiment. Parameters are listed in Table 3. After that, MPM calculates particle dipoles at a range of frequencies and streamlines the output to compute the measured variables. The analysis of KK-res is a bit different for this study. The particle dipoles at low- and high-frequency limit and the ensemble extinction spectrum are computed. Before obtaining measured variables that are dependent on light frequency, the particle dipoles $C_i(\omega)$ at each frequency are required, which are calculated according to Appendix A.

	IO	3% ITO	8.4% ITO
$\omega_{p,i}$ (cm^{-1})	0	12313	16018
γ_i (cm^{-1})	–	681	1602
$\varepsilon_{\infty,i}$ (ε_0)	1.88	1.88	4

Table 3: Drude parameters of indium oxide (IO) and 3% and 8.4% tin-doped indium oxide (ITO).

Effective refractive index n_{eff} is the major optical property of the IO and 3% ITO sample and is measured in experiment and simulated by MPM in Kim et al. Physically, it shows the ensemble frequency-dependent refractive index of the two-dimensional superlattice when the incident light is perpendicular to surface. It is calculated as

$$n_{eff} = \sqrt{\varepsilon_{eff}} = \sqrt{\varepsilon_f + n \sum_j C_j(\omega)} \tag{33}$$

where ε_{eff} is effective permittivity and $n = N/V$ is the number density associated with the simulation box volume. In our study here, we compare the effective refractive index computed by KK-res and the original MPM data. Subsequently, we compute reflectance and transmittance in response to an incident light perpendicular to the surface to demonstrate the usage of KK-res in simulating other optical quantities. The simulation approach of reflectance and transmittance assumes the surface exists in air without supporting substrate like Si, then we solve the Maxwell equations at each boundary and medium in the system. Finally, the relationship is

$$R_p = |E_{r,p}|^2, \quad T_p = |E_{t,p}|^2 \tag{34}$$

where R_p and T_p are reflectance and transmittance with in-plane polarization and $E_{r,p}$ and $E_{t,p}$ are the electric field coefficient associated with reflectance and transmittance.

KK-res has achieved a high accuracy due to the fixed particle positions in a hexagonal lattice, which is shown in Figure 5A-D. As the mixing ratio of IO over 3% ITO increases, meaning there is more IO in sample, the resonant peak feature disappears because IO is dielectric and does not obtain any localized surface plasmon resonance (LSPR) mode, while the plasmonic ITO does. The result shows that KK-res can capture the measurable optical properties in mixture that has different components. In addition, different resonance shifts from anisotropic structure can be characterized by KK-res. In Figure 5E, when light shines on the simulated superlattice surface in the unit directions, the nanoparticles resonate at distinct resonance frequencies and shift to opposite directions according to different mixing ratios. Since the in-plane incident electric field induces a strong coupling between ITO nanoparticles with perpendicular light, the resonance frequency is red-shifted. On the other hand, more ITO will respond to the out-of-plane electric field with less coupling effect, so the resonance frequency blue-shifted instead. In Figure 5F, mean-field approximation only shows a single set of extinction spectra because it has no structural information and it assumes the configuration is always isotropic; hence the inaccurate prediction.

We have discussed the case composed of IO and 3% ITO, a mixture of dielectric and plasmonic

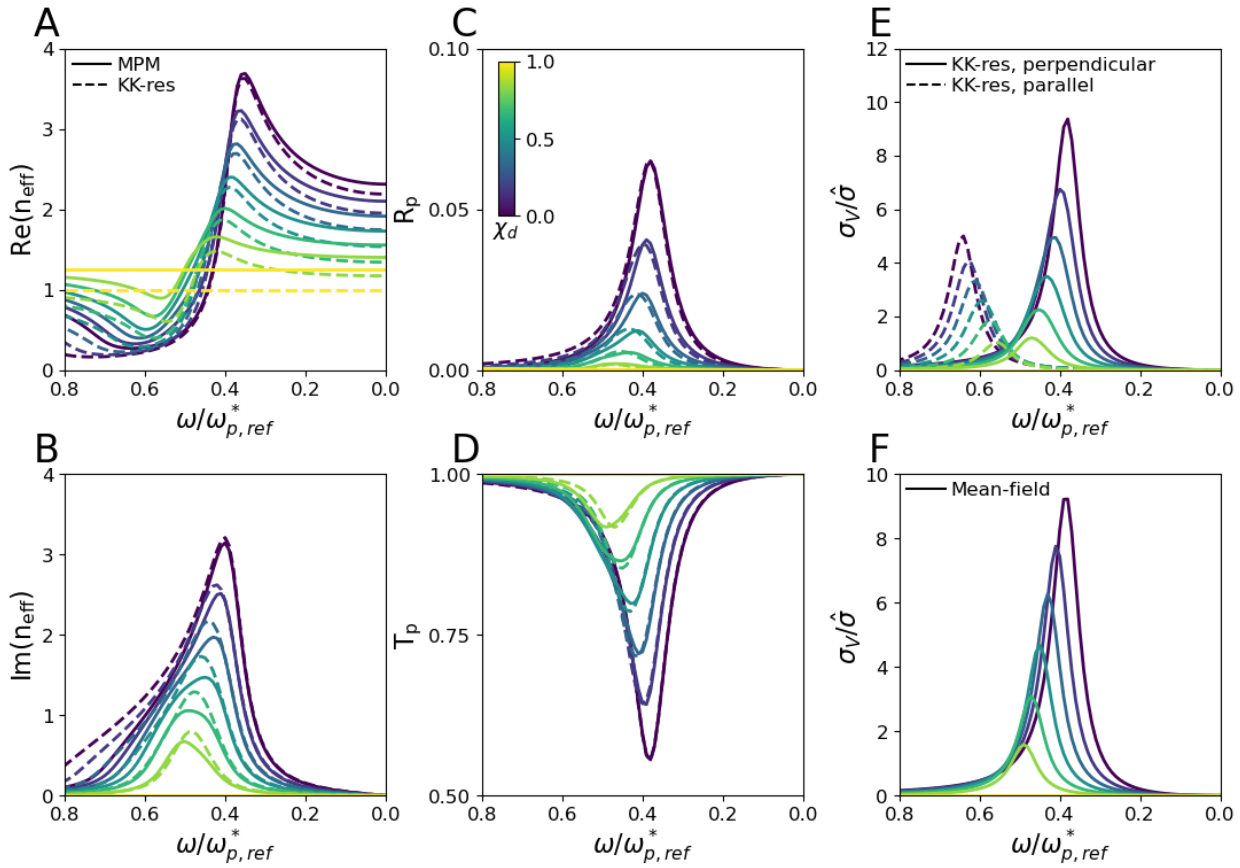

Figure 5: (A) Real and (B) imaginary part of effective refractive index, (C) reflectance and (D) transmittance in response to perpendicular incident light to a two-dimensional, hexagonal IO/3% ITO superlattice surface at multiple mixing ratio. The experiment (solid) curves are taken from the original MPM data provided by Kim et al. The KK-res (dashed) curves display a fairly accurate prediction on all quantities. Extinction spectra are shown for (E) KK-res with incident light perpendicular (solid) and parallel (dashed) to the surface, and (F) mean-field approximation which does not display any anisotropic result.

nanoparticles. What about a case with 2 distinct plasmonic nanoparticles? Our simulation with KK-res is able to model it with the current setup. However, featuring multiple peaks in the ensemble extinction spectrum poses a challenge as the peak function always predicts that there is one resonant peak. With more resonant mode, the error accumulates fast and so KK-res performs sub-optimally for multiple plasmonic mixtures.

7 Usage of KK-res with Other Dielectric Model

In our final example, we look at the usage of KK-res with a dielectric model other than Drude. With a different dielectric permittivity function, the peak function might be altered and the integral in Eq. (26) might not be able to be evaluated analytically. However, we prove that with core-shell function consisted of a Drude core and a dielectric shell, the formulation is the same as pure Drude.

$$\varepsilon_{p,i}(\omega) = \varepsilon_{s,i}\frac{\varepsilon_{c,i} + 2\varepsilon_{s,i} + 2\phi_c(\varepsilon_{c,i} - \varepsilon_{s,i})}{\varepsilon_{c,i} + 2\varepsilon_{s,i} - \phi_c(\varepsilon_{c,i} - \varepsilon_{s,i})} \tag{35}$$

where $\varepsilon_{c,i}$ and $\varepsilon_{s,i}$ is core/shell permittivity and ϕ_c is volume fraction of core corresponded to particle volume. To demonstrate the credibility of the claim and the extensive application of KK-res, we reproduce another published experimental study conducted by Kang et al. [24] The configuration is composed of core-shell nanoparticles assembled in a three-dimensional, highly clustered network interacting with strong attractive depletion force. The core is 8.4% ITO described by Drude model with parameters in Table (3) and the shell is ligand that has a constant permittivity.

Instead of extinction spectra, we decide to show the result in form of a plasmon ruler. Plasmon ruler shows the resonant peak shift compared to the isolated, non-coupling case as a function of separation between nanoparticle cores. The principle is similar to the first simulation study with weakly attractive fluid. As the gap between nanoparticle cores decreases from increasing core size (larger ϕ_c), the coupling component that is the nanoparticle core becomes closer to one another and thus the resonance frequency is more red-shifted. Figure 6 demonstrates this with the decreasing trends across all sampled shell permittivity. Due to the nondimensionalized unit of $\varepsilon_f = 2.04\varepsilon_0$, $\varepsilon_{s,i} = 1$ refers to that the shell permittivity equals to background permittivity, essentially rendering the shell as invisible; $\varepsilon_{s,i} = 4/2.02 \approx 2$ means that the shell permittivity equals to the high-frequency limit permittivity $\varepsilon_{\infty,i}$.

Having established the correlation between plasmon resonance shift and core gap distance. The plasmon ruler can effectively serve as a predictive model in optical property design. In positional design of an optical device, we can use spectroscopy to measure extinction cross-section

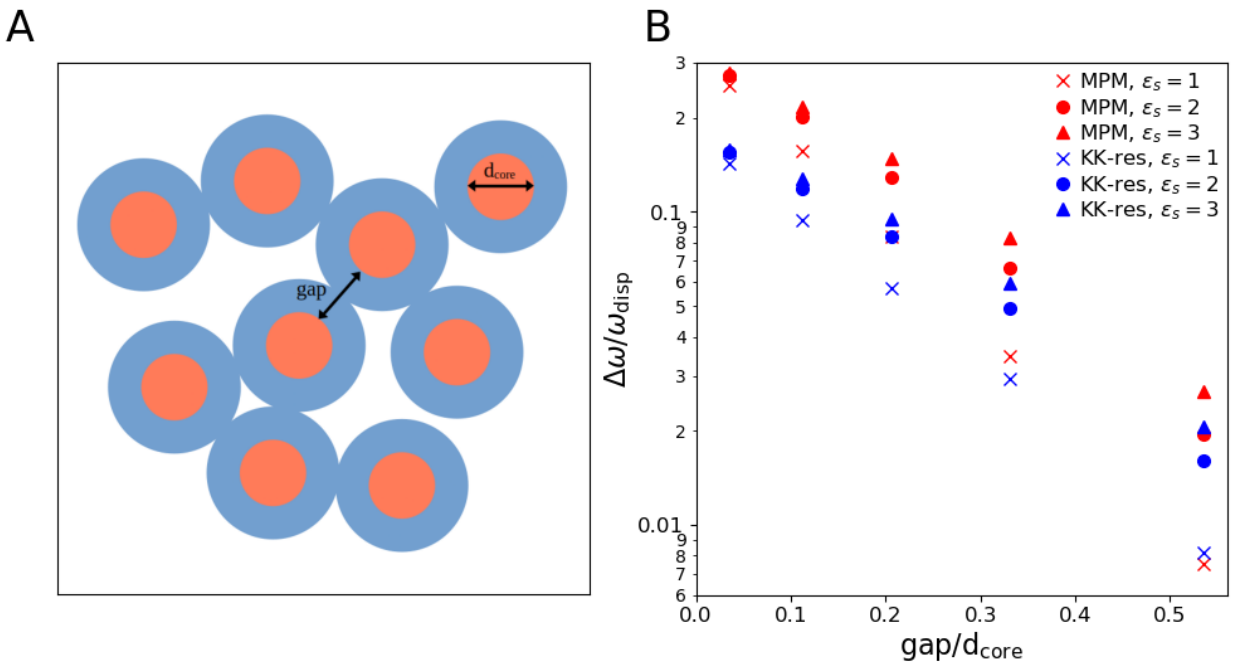

Figure 6: (A) Definition of a gap between plasmonic cores and its unit particle diameter d_{core} in a percolated network of core-shell particles. (B) Plasmon ruler with simulated normalized plasmon resonance shift ($\Delta\omega/\omega_{disp}$) as a function of normalized gap distance (gap/d_{core}) with multiple shell permittivity $\varepsilon_{s,i}$. The diminishing trend shows that the extinction spectra are less red-shifted as the core separation increases.

per nanoparticle volume and convert them into resonant peak shift of the fabricated sample. Then apply the plasmon ruler to obtain the average gap distance between plasmonic nanoparticles. By contrast, if we know the gap separation from scanning electron spectroscopy (SEM), the model can predict the resonance shift. Therefore, the plasmon ruler is useful in both forward and inverse design process.

8 Conclusion and Future Work

By proposing the Kramers-Kronig resonance frequency approximation, we enable a more rapid simulation workflow involving fewer computation steps compared to the pre-existed MPM. For example, a potential application is inverse designing a metamaterial with a certain optical property. Starting at an arbitrary set of initial parameters, the analyticity of KK-res provides a fairly high fidelity result computed on the large particle configuration. Then, combining the converged parameters and MPM can generate a final, simulated structure design with fewer iterations over a shorter time period. Another example is simulating a high-throughput material screening. With other methods, we are limited by the number of nanoparticles and computation speed. Nevertheless, KK-res can loop through a permutation of variables in a multi-dimensional space and calculate optical response with a correct parallelization. It advances the simulation approach in massive plasmonic nanoparticle assemblies by an order of magnitude.

Potential continuation of the KK-res approximation includes implementing the method using GPU-accelerated algorithm and relaxing the quasistatic assumption. The current procedure is only optimized for running on CPU exclusively. Harnessing the power of GPU and the Nvidia CUDA framework, all fast Fourier transforms and matrix inversions in computing particle dipoles can be parallelized with multithreading. This provides another order-of-magnitude acceleration to the algorithm of the mutual dipole approximation. Quasistatic limit assumption mainly constrains the particle size and incident light frequency. Accounting the additional mechanisms will allow us to simulate cases that are easily repeatable in experiments and increase the versatility of the method. Since I am continuing as a Ph.D. student in the Sherman group, these tasks will be my future goals in the time at University of Washington.

9 Acknowledgements

All the work presented in this thesis would not be possible without my incredible research advisor Professor Zach Sherman. His endless knowledge and passion in the field motivates me to strive for the best in this project. His patience in teaching me complicated concepts in optics is immensely helpful to me in understanding the subject. I would also like to thank Ayça Ersoy, Rishabh Sanghavi, Haoqing Zhang, Hanson Chen, Yu-Fang Hsieh, who are my fellow Ph.D. students in the Z Lab, and Professor Lilo Pozzo's lab. I appreciate all your ideas and feedback on formulating my project. I had a great opportunity to work closely with two undergraduate students, Kyla Yamamoto and Varad Mudvikar, in my two-year Master program. I appreciate all your time put into the project and your patience working with me as a first-time mentor. Finally, I want to thank Dr. Kristen Finch, staff scientist at UW-IT, for answering all my Hyak-related questions throughout my journey at UW. I learned a lot about supercomputing from you.

References

[1] V. Amendola, R. Pilot, M. Frasconi, O. M. Maragò, and M. A. Iatì, "Surface plasmon resonance in gold nanoparticles: a review", en, Journal of Physics: Condensed Matter **29**, Publisher: IOP Publishing, 203002 (2017).

[2] J. Yan, X. Liu, C. Ma, Y. Huang, and G. Yang, "All-dielectric materials and related nanophotonic applications", en, Materials Science and Engineering: R: Reports **141**, 100563 (2020).

[3] S. Mitra and M. Basak, "Diverse bio-sensing and therapeutic applications of plasmon enhanced nanostructures", Materials Today **57**, 225–261 (2022).

[4] P. Wang, M. E. Nasir, A. V. Krasavin, W. Dickson, Y. Jiang, and A. V. Zayats, "Plasmonic Metamaterials for Nanochemistry and Sensing", Accounts of Chemical Research **52**, Publisher: American Chemical Society, 3018–3028 (2019).

[5] L. Mascaretti, Y. Chen, O. Henrotte, O. Yesilyurt, V. M. Shalaev, A. Naldoni, and A. Boltasseva, "Designing Metasurfaces for Efficient Solar Energy Conversion", ACS Photonics **10**, Publisher: American Chemical Society, 4079–4103 (2023).

[6] J. Kim, G. V. Naik, A. V. Gavrilenko, K. Dondapati, V. I. Gavrilenko, S. M. Prokes, O. J. Glembocki, V. M. Shalaev, and A. Boltasseva, "Optical Properties of Gallium-Doped Zinc Oxide—A Low-Loss Plasmonic Material: First-Principles Theory and Experiment", en, Physical Review X **3**, 041037 (2013).

[7] M. C. Mathpal, P. Kumar, A. K. Tripathi, R. Balasubramaniyan, M. K. Singh, J. S. Chung, and A. Agarwal, "Facile deposition and plasmonic resonance of Ag–Au nanoparticles in titania thin film", en, New Journal of Chemistry **39**, 6522–6530 (2015).

[8] J. A. Fan, C. Wu, R. Bardhan, N. J. Halas, V. N. Manoharan, P. Nordlander, G. Shvets, and F. Capasso, "Self-Assembled Plasmonic Nanoparticle Clusters", en, Science **328**, 1135–1138 (2010).

[9] Y. Bao, B. Zhao, D. Hou, J. Liu, F. Wang, X. Wang, and T. Cui, "The redshift of surface plasmon resonance of colloidal gold nanoparticles induced by pressure with diamond anvil cell", en, Journal of Applied Physics **115**, 223503 (2014).

[10] Z. M. Sherman, K. Kim, J. Kang, B. J. Roman, H. S. N. Crory, D. L. Conrad, S. A. Valenzuela, E. Lin, M. N. Dominguez, S. L. Gibbs, E. V. Anslyn, D. J. Milliron, and T. M. Truskett, "Plasmonic Response of Complex Nanoparticle Assemblies", Nano Letters **23**, 3030–3037 (2023).

[11] Z. M. Sherman, H. Rosenthal, and J. W. Swan, "Phase Separation Kinetics of Dynamically Self-Assembling Nanoparticles with Toggled Interactions", Langmuir **34**, Publisher: American Chemical Society, 1029–1041 (2018).

[12] W. B. Russel, P. M. Chaikin, J. Zhu, W. V. Meyer, and R. Rogers, "Dendritic Growth of Hard Sphere Crystals", Langmuir **13**, Publisher: American Chemical Society, 3871–3881 (1997).

[13] W. B. Russel, D. A. Saville, and W. R. Schowalter, *Colloidal Dispersions*, en (Cambridge University Press, 1989).

[14] S. Kim and S. J. Karrila, *Microhydrodynamics: Principles and Selected Applications*, en (Dover Publications, June 2005).

[15] D. Heyes and J. Melrose, "Brownian dynamics simulations of model hard-sphere suspensions", en, Journal of Non-Newtonian Fluid Mechanics **46**, 1–28 (1993).

[16] S. Asakura and F. Oosawa, "On Interaction between Two Bodies Immersed in a Solution of Macromolecules", en, The Journal of Chemical Physics **22**, 1255–1256 (1954).

[17] J. A. Anderson, C. D. Lorenz, and A. Travesset, "General purpose molecular dynamics simulations fully implemented on graphics processing units", en, Journal of Computational Physics **227**, 5342–5359 (2008).

[18] C. L. Phillips, J. A. Anderson, and S. C. Glotzer, "Pseudo-random number generation for Brownian Dynamics and Dissipative Particle Dynamics simulations on GPU devices", en, Journal of Computational Physics **230**, 7191–7201 (2011).

[19] J. Glaser, T. D. Nguyen, J. A. Anderson, P. Lui, F. Spiga, J. A. Millan, D. C. Morse, and S. C. Glotzer, "Strong scaling of general-purpose molecular dynamics simulations on GPUs", en, Computer Physics Communications **192**, 97–107 (2015).

[20] S. Eustis and M. A. El-Sayed, "Why gold nanoparticles are more precious than pretty gold: Noble metal surface plasmon resonance and its enhancement of the radiative and nonradiative properties of nanocrystals of different shapes", en, Chem. Soc. Rev. **35**, 209–217 (2006).

[21] D. Lindbo and A.-K. Tornberg, "Spectral accuracy in fast Ewald-based methods for particle simulations", en, Journal of Computational Physics **230**, 8744–8761 (2011).

[22] J. S. Toll, "Causality and the Dispersion Relation: Logical Foundations", Physical Review **104**, 1760–1770 (1956).

[23] K. Kim, Z. M. Sherman, A. Cleri, W. J. Chang, J.-P. Maria, T. M. Truskett, and D. J. Milliron, "Hierarchically Doped Plasmonic Nanocrystal Metamaterials", Nano Letters **23**, Publisher: American Chemical Society, 7633–7641 (2023).

[24] J. Kang, Z. M. Sherman, D. L. Conrad, H. S. N. Crory, M. N. Dominguez, S. A. Valenzuela, E. V. Anslyn, T. M. Truskett, and D. J. Milliron, "Structural Control of Plasmon Resonance in Molecularly Linked Metal Oxide Nanocrystal Gel Assemblies", ACS Nano **17**, Publisher: American Chemical Society, 24218–24226 (2023).

A Estimating particle dipoles at arbitrary frequency with KK-res

To compute quantities other than extinction cross-section per nanoparticle volume $\sigma_V(\omega)$, we first need to know particle capacitance $C_i(\omega)$ at any arbitrary frequency. Therefore, with the extinction spectrum known, we start with the Kramers-Kronig relation, Eq. (18), and substitute in function $C_{D,i}(\omega)$.

$$C'_{D,i}(\omega) = \frac{2}{\pi} P \int_0^\infty d\omega' \, \frac{\omega' C''_{D,i}(\omega')}{\omega'^2 - \omega^2} \tag{36}$$

Evaluate $C_{D,i}(\omega) = C_i(\omega) - C_i(\infty)$ and Eq. (25).

$$C'_i(\omega) - C_i(\infty) = \frac{2\sqrt{\varepsilon_f}}{\pi\sqrt{\mu_f}} P \int_0^\infty d\omega' \, \frac{\sigma_i(\omega')}{\omega'^2 - \omega^2} \tag{37}$$

Plug in the peak function Eq. (17) for σ_i and nondimensionalize with $\widetilde{\omega} = \omega/\omega_{res,i}$, $\widetilde{W_i} = W_i/\omega_{res,i}$, and $x = \omega'/\omega_{res,i}$.

$$C'_i(\omega) - C_i(\infty) = \frac{2\sqrt{\varepsilon_f}}{\pi\sqrt{\mu_f}} \frac{h_i W_i^2}{\omega_{res,i}^3} I(\widetilde{\omega}; \widetilde{W_i}), \tag{38}$$

$$I = P \int_0^\infty dx \frac{x^2}{(x+\widetilde{\omega})(x-\widetilde{\omega})\left(1 + \left(\widetilde{W_i^2} - 2\right) x^2 + x^4\right)} \tag{39}$$

Now we need to solve the integral to obtain an analytical expression. Note that the integrand $g(x)$ is an even function satisfying $g(x) = g(-x)$ because it involves only even powers of x. Therefore, we can extend the lower bound of the integral to $-\infty$.

$$I = \frac{1}{2} P \int_{-\infty}^\infty dx \frac{x^2}{(x+\widetilde{\omega})(x-\widetilde{\omega})\left(1 + \left(\widetilde{W_i^2} - 2\right) x^2 + x^4\right)} \tag{40}$$

We use analytic continuation to extend $g(x) \to g(z)$ into the complex plane. The integral of $g(z)$ is then evaluated over the closed contour $C = C_0 + C_1 + C_2 + C_\infty$ as indicated in Figure 7.

Start with C_∞, which is a semicircle of radius R. Since the integrand decays as $g \sim 1/|z|^4$,

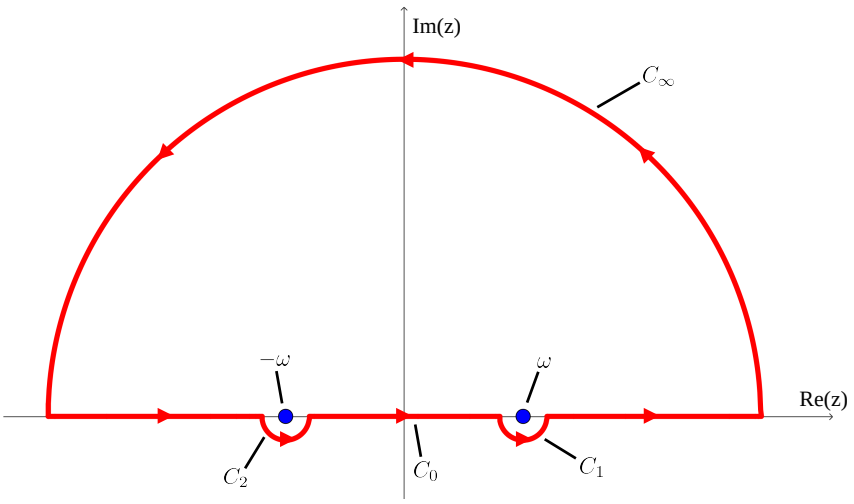

Figure 7: The line integral contour of $g(z)$.

so on C_∞ it is $g \sim 1/R^4$. In the limit of $R \to \infty$, this integral vanishes.

$$I_{C_\infty} = \int_{C_\infty} dz\, g(z) = 0 \tag{41}$$

Now for the integral over C_1. Apply a polar representation to center the integral around the pole $z = \widetilde{\omega}$

$$z - \widetilde{\omega} = \delta e^{i\phi}, \quad dz = i\delta e^{i\phi} d\phi \tag{42}$$

The integral over C_1 in terms of ϕ becomes

$$I_{C_1} = \int_\pi^{2\pi} d\phi \, \frac{(\widetilde{\omega} + \delta e^{i\phi})^2 i\delta e^{i\phi}}{(1 + (\widetilde{W}_i^2 - 2)(\widetilde{\omega} + \delta e^{i\phi})^2 + (\widetilde{\omega} + \delta e^{i\phi})^4)(2\widetilde{\omega} + \delta e^{i\phi})\delta e^{i\phi}} \tag{43}$$

Sending $\delta \to 0$ to approach the pole and simplify

$$I_{C_1} = \int_\pi^{2\pi} d\phi \, \frac{i\widetilde{\omega}}{2(1 + (\widetilde{W}_i^2 - 2)\widetilde{\omega}^2 + \widetilde{\omega}^4)} = \frac{i\pi\widetilde{\omega}}{2(1 + (\widetilde{W}_i^2 - 2)\widetilde{\omega}^2 + \widetilde{\omega}^4)} \tag{44}$$

Similarly, repeat the operation for the integral over C_2, which is around the pole $z = -\widetilde{\omega}$.

$$I_{C_2} = -\frac{i\pi\widetilde{\omega}}{2(1 + (\widetilde{W}_i^2 - 2)\widetilde{\omega}^2 + \widetilde{\omega}^4)} \tag{45}$$

Therefore, the integral over $C_1 + C_2$ vanishes

$$I_{C_1} + I_{C_2} = 0 \tag{46}$$

The integral over C_0 (i.e. $2I$) is equal to the integral over the entire C. $g(z)$ has 6 poles total and 4 of them are inside C at

$$z_1 = \widetilde{\omega},\ z_2 = -\widetilde{\omega},\ z_3 = \sqrt{\frac{2 - \widetilde{W}_i^2 + \widetilde{W}_i\sqrt{\widetilde{W}_i^2 - 4}}{2}},\ z_4 = -\sqrt{\frac{2 - \widetilde{W}_i^2 - \widetilde{W}_i\sqrt{\widetilde{W}_i^2 - 4}}{2}} \tag{47}$$

Hence, the integral over C is given by the residue theorem.

$$\int_C dx\, g(x) = \int_{C_0} dx\, g(x) = 2I = 2\pi i \sum_j \operatorname{Res} g(z_j) \tag{48}$$

Evaluate Eq. (48) and simplify

$$I = \frac{\pi(1 - \widetilde{\omega}^2)}{2\widetilde{W}_i(1 + (\widetilde{W}_i^2 - 2)\widetilde{\omega}^2 + \widetilde{\omega}^4)} \tag{49}$$

Plugging into Eq. (38) and restore the nondimensionalization.

$$C_i'(\omega) - C_i(\infty) = \frac{\sqrt{\varepsilon_f}}{\sqrt{\mu_f}} \frac{h_i W_i}{\omega_{res,i}^2} \frac{1 - \left(\dfrac{\omega}{\omega_{res,i}}\right)^2}{\left(\dfrac{\omega}{\omega_{res,i}}\right)^4 + \left(\left(\dfrac{W_i}{\omega_{res,i}}\right)^2 - 2\right)\left(\dfrac{\omega}{\omega_{res,i}}\right)^2 + 1} \tag{50}$$

Lastly, with Eq. (27), the real part of particle capacitance at any frequency is related to the capacitance at low- and high-frequency limit.

$$C_i'(\omega) - C_i(\infty) = (C_i(0) - C_i(\infty)) \frac{1 - \left(\dfrac{\omega}{\omega_{res,i}}\right)^2}{\left(\dfrac{\omega}{\omega_{res,i}}\right)^4 + \left(\left(\dfrac{W_i}{\omega_{res,i}}\right)^2 - 2\right)\left(\dfrac{\omega}{\omega_{res,i}}\right)^2 + 1} \tag{51}$$

Since the extinction spectrum is known, using Eq. (25), we can obtain the imaginary part of particle capacitance $C_i''(\omega)$ and thus the full dipole value $C_i(\omega)$.